Laboratory Characterization and Modeling of a Near-Infrared Enhanced Photomultiplier Tube

A. Biswas[1] and W. H. Farr[1]

The photon-starved channel for optical communications from deep space requires the development of detector technology that can achieve photon-counting sensitivities with high bandwidth. In this article, a near-infrared enhanced photomultiplier tube (PMT) with a quantum efficiency of 0.08 at a 1.06-μm wavelength is characterized in the laboratory. A Polya distribution model is used to compute the probability distribution function of the emitted secondary photoelectrons from the PMT. The model is compared with measured pulse-height distributions with reasonable agreement. The model accounts for realistic device parameters, such as the individual dynode stage gains and a shape parameter that is representative of the spatial uniformity of response across the photocathode and dynodes. Bit-error rate (BER) measurements also are presented for 4- and 8-pulse-position modulation (PPM) modulation schemes with data rates of 20 to 30 Mb/s. A BER of 10^{-2} is obtained for a mean of 8 detected photons.

I. Introduction

Laser communications over planetary distances will boost data transfer rates by at least an order of magnitude over present radio-frequency-based techniques. In the envisioned scenarios, the huge space loss of a laser beam propagating over planetary distances must be overcome under a spacecraft-resource-limited average-laser-power constraint. By tailoring the laser duty cycle to transmit temporally narrow high-peak-power pulses, multiple bits of information per laser pulse may be transmitted using a pulse-position modulation (PPM) scheme, whereby $\log_2 M$ bits of data are encoded by the temporal position of the pulse in a "symbol" time comprised of M-slots. This allows the trading of channel efficiency (bits/photon) for channel capacity (bits/second) under the average-laser-power constraint.

PPM requires an efficient laser capable of emitting temporally narrow high-peak-power pulses. Neodymium-doped crystal lasers emitting near 1 μm in the near-infrared meet this requirement. The pulse output requirement can be met by running the laser in a Q-switched mode. However, Q-switching is limited to a maximum pulse-repetition frequency (PRF) of a few hundred kilohertz, which

[1] Communications Systems and Research Section.

The research described in this publication was carried out by the Jet Propulsion Laboratory, California Institute of Technology, under a contract with the National Aeronautics and Space Administration.

correspondingly limits the maximum PPM symbol rate. For higher PRFs, cavity dumping or pulsed fiber amplifiers are being considered.

Therefore, efficient detection in the 1-μm region of the optical spectrum is desirable to match a neodymium laser wavelength. From a device standpoint, this is an interesting spectral regime since it is close to the tail of the silicon spectral absorption. Here the inherent quantum efficiency is reduced to a few percent, and only a small fraction of incident photons is detected. However, other materials that do display higher quantum efficiencies in this region are plagued by poorer noise characteristics.

Assuming an Earth-based receiver antenna, sunlight scattered from the atmosphere (sky radiance) contributes additive background noise during daytime optical links. The sky radiance at a particular site depends upon the Sun-to-receive telescope-to-laser transmitter angle, the Sun zenith angle, the altitude above mean sea level, and other site-specific atmospheric parameters, such as aerosol content. For a given-diameter receiving antenna at a particular site, the variance of additive background noise is directly proportional to (1) the bandpass of the optical filter used, (2) the effective solid angle of the signal detector, and (3) the temporal slot width of the PPM scheme. Reducing any of these will reduce additive background noise. The optical filter bandpass is limited by the laser line width and the Doppler shifts it is subjected to, typically on the order of 1 Å. The effective solid angle (field-of-view) is limited by atmospheric turbulence. The temporal slot width is limited by the laser pulse width and jitter. However, the detector response time (bandwidth) may instead limit the practically realizable slot width.

The deep-space optical communications channel is predicated to be photon-starved per the average-laser-power constraint. Photon counting, therefore, is the best technique for efficient detection. Although post-detector additive thermal noise can be minimized by careful electronics design, some internal gain within a photon-counting detector is mandatory for overcoming inherent $k \times T \times C$ thermal noise, k being the Boltzmann constant, T the noise temperature, and C the capacitance. The detector bandwidth should be equal to or greater than the laser pulse bandwidth. The detector output must provide a "raw" (uncoded) word-error rate (WER) that is compatible with PPM slot-, symbol-, and frame-synchronization algorithms, typically 10^{-2}, although operating points with higher acceptable error probabilities have been identified through analysis and simulation. Also, efficient coding algorithms to reduce the final bit-error rate (BER) to less than 10^{-6} require that the detector produce an output signal that is proportional to the received pulse photon number.

The detector diameter should match the atmospheric-turbulence-limited solid angle for efficient collection of the received photon signal. There is a trade-off here, because increasing the detector area increases additive background noise, decreases the detector bandwidth, and increases detector noise due to increasing device capacitance. Finally, a most important requirement for the preferred detector is a high quantum efficiency (QE) to convert the largest fraction of incident photons into photoelectrons.

Some of the more popular single photon-counting devices are photomultiplier tubes (PMTs), avalanche photodiodes (APDs) operating in either proportional or Geiger (avalanche) mode, hybrid PMTs, and solid-state photomultipliers (SSPMs). More recently, "hot" electron superconducting single photon detectors have been reported. A careful survey of these devices shows that no single device presently satisfies all of the above requirements for a deep-space optical communications ground detector. See Table 1 for a summary of the devices discussed.

In this article, we describe the results of laboratory tests of a near-infrared (NIR) enhanced liquid-nitrogen-cooled PMT. This device is selected from those in Table 1 to demonstrate the applicability of a photon-counting detector for a deep-space optical communications receiver. Its high internal gain minimizes requirements for post-detector amplification; it offers moderate bandwidth with a large detection area, has an output proportional to the input photon number, and a reasonable (although low) quantum efficiency at the 1.06-μm neodymium laser wavelength. Test results are compared with idealized predictions and PMT models. In previous work [1,2], laboratory results using photon-counting PMTs have been

Table 1. A comparison of available photon-counting detectors.

Technology	Cooling, K	Quantum efficiency at 1064 nm, percent	Response time, ns	Wavelength, nm	Dark rate, kcycles/s	Gain	Area, mm^2	Notes
NIR PMT	77	8	9	300–1700	20–200	1×10^6	>20	2-μA anode current limit
Hybrid PMT	<300	15	1	900–1300	50	12×10^3	1	—
SSPM	<10	1 (front) 20 (edge)	3	400–2800	7	20×10^3	1	No excess noise, 3×10^7 max rate
Si APD (Geiger mode)	<280	18	<10	350–1000	0.250	∞	0.2	Requires pulse quenching
Si APD (gain mode)	<200	40	2	350–1000	10	$> 1 \times 10^3$	9	—
InGaAs APD (gain mode)	150–200	60	1	900–1500	500	20×10^3	0.01	—
Hot-electron NbN	4–10	2	0.03	400–2000	10^{-4}	3×10^2	0.0001	Polarization sensitive

used to evaluate the performance expected for a deep-space optical communications link. A modulated diode laser operating at a 0.85-μm wavelength, where the PMT quantum efficiency was 15 percent, was used. A 2.5-bits/photon capability was demonstrated for uncoded data rates of 312 kbits/second using 256-PPM and 100-ns slots. As elaborated below, in the current work a diode laser with an output wavelength of 1.07 μm with a PMT quantum efficiency of 0.08 is used. The PPM slot widths are from 6 to 16 ns, and the data rates approach 20 to 30 Mb/s with 4- and 8-PPM. The performance achieved was 0.25 to 0.42 bits/photon.

In Section II, we present PMT models, while in Section III the experimental arrangement used is described. Section IV presents the experimental results and a comparison to predicted pulse-height distribution, and Section V is the conclusion.

II. Photomultiplier Tube Models

Photomultiplier tubes (PMTs) approach ideal photon-counting detectors because of their high internal gain and low dark noise. A PMT consists of a vacuum enclosure with a photocathode followed by a daisy chain of dynodes culminating in an anode. A stepped potential gradient applied across the dynode chain accelerates primary photoelectrons ejected from the photocathode towards the anode. Thus, a single primary photoelectron generated due to absorption of a single photon will collide with the first dynode stage, causing a cascade of secondary electrons to be ejected. The process continues at each successive dynode stage, generating a high internal gain, so that from 10^5 to 10^6 electrons arrive at the anode. For metal photocathodes, the threshold that must be exceeded by the incident photons is the work function, whereas for semiconductor materials, the threshold is better approximated by the electron-affinity energy. The initial emission of the primary photoelectrons followed by the subsequent gain stages is a good example of a branching process used to characterize phenomena ranging from cosmic ray showers to nuclear chain reactions.

The noiseless gain process referred to above is less than ideal by virtue of the fact that the gain is not fixed but exhibits some variance about a mean value. The ratio of the variance to the square of the mean is a figure of merit of the device, also known as the excess noise. In a previous article [3], the variance

in the gain of a PMT was approximated using a Markov diffusion process. In a subsequent article [4], the difficulties in evaluating the expression resulting from the Markov approximation were emphasized, and it was shown that a gamma distribution provided an easier means of computing the probability distribution function of gain while producing results that were in almost exact agreement with the more computationally cumbersome Markov diffusion model. Both of these models, however, treat the PMT as a "black box" and, besides the mean gain of the PMT, no other device parameter dependence is invoked in these models.

Older PMT models [5] were derived using the discrete Polya statistical model to describe the emission of photoelectrons from a single stage. The Polya distribution [6] for a single stage of gain is described by

$$P(n) = \frac{\mu^n}{n!}\,(1+b\mu)^{-n-(1/b)} \prod_{i=1}^{n-1}(1+ib) \tag{1}$$

where $P(n)$ is the probability of emitting n electrons, μ is the mean gain, and b is a shape parameter. The generating function for the Polya distribution is given by

$$G(s) = \left[1+b\mu(1-s)\right]^{-1/b} \tag{2}$$

It can be shown [7] that, as $b \to 0$, taking the natural logarithm of both sides of Eq. (2) and expanding $\ln[1+b\mu(1-s)]^{-1/b}$ in a Taylor series about $b = 0$ results in the generating function for a Poisson distribution, $\ln[G(s)] = \mu(s-1)$. On the other hand, $b = 1$ results in an exponential distribution. Thus, b acts as a shape parameter, allowing the distribution to represent an exponential on one extreme and a Poisson on the other. Physically, b has been interpreted as the uniformity of the gain across the surface of the photoelectron emitting device. The more uniform the emission characteristics of the surface, the more Poisson-like the distribution will be, and as the non-uniformity of the gain across the surface increases, the more exponential will be the resulting distribution.

Figure 1(a) provides a conceptual view of the gain stages in a PMT. For the very first stage, shown with a dashed border, gain equal to the mean number of incident photons times the quantum efficiency of the PMT is assumed. Gain of the subsequent stages is assigned according to the distribution shown in Fig. 1(b) as specified in the manufacturer's data sheet.

The Polya distribution model is used to model the pulse-height distribution at the anode. Note that, in contrast to the models presented in [3] and [4], the Polya model allows real device parameters such as the stage gains to be accounted for. Moreover, varying the value of b for each stage can in principle assess the spatial uniformity of gain for each stage.

Thus, for a J-dynode stage device, the generating functions for the Polya distribution can be written as

$$\left.\begin{aligned} G_J(s) &= \left\{1+b_1\mu_1\left[1-G_{J-1}(s)\right]\right\}^{-1/b_1} \\ G_{J-1}(s) &= \left\{1+b_2\mu_2\left[1-G_{J-2}(s)\right]\right\}^{-1/b_2} \\ &\vdots \\ G_1(s) &= \left\{1+b_J\mu_J[1-s]\right\}^{-1/b_J} \end{aligned}\right\} \tag{3}$$

(a)

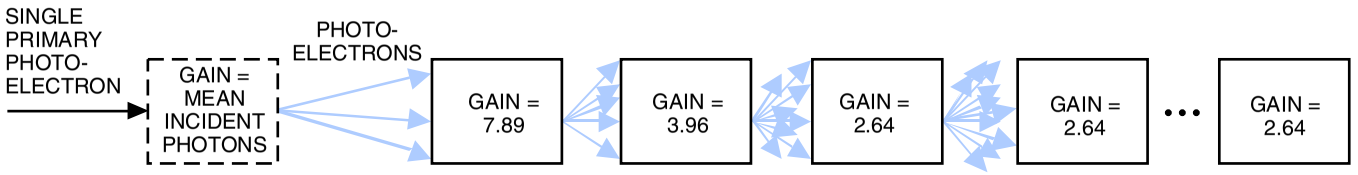

(b)

K = PHOTOCATHODE, B = BIAS, Dy1 ⋯ 10 = DYNODES, P = ANODE

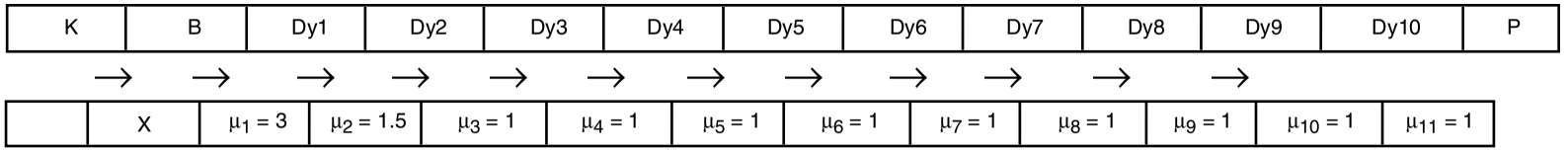

Fig. 1. PMT: (a) a schematic view of the gain stages in a PMT and (b) the distribution of gain as reported for the PMT used in the current work; using this, the gain per stage shown in Fig. 1(a) was obtained.

In [6], a recursion relationship was derived for obtaining the probability distribution from the generating functions. Thus, for the general case of a J-stage device, the recursion formula can be written so that $P(n;K,l)$, the probability of producing n electrons after K consecutive gain stages within a J-stage device, with $K = J - l + 1$, is given by

$$P(n;K,l) = \frac{\mu_l}{n}\left[P(0;K,l)\right]^{b_l}\sum_{i=0}^{n-1}\left[n + i(b_l - 1)\right]xP(i;K,l)xP(n-i;K-1,l+1),$$

$$n \geq 1, l \leq K \leq J, 1 \leq l \leq J \tag{4a}$$

where

$$P(0;K,l) = \left\{1 + b_l\mu_l\left[1 - P(0;K-1,l+1)\right]\right\}^{-1/b_l}$$

$$n = 0, l \leq K \leq J, 1 \leq l \leq J \tag{4b}$$

For $b = 0$ that is spatially uniform dynode stages with a cascade of pure Poisson stages, Eq. (4) reduces to

$$P(n;K,l) = \frac{\mu_l}{n}\sum_{i=0}^{n-1}(n-i)P(i;K,l)P(n-i;K-1,l+1)$$

$$n \geq 0, K \geq 1, 1 \leq l \leq J \tag{5a}$$

$$P(0;K,l) = P_1\left\{P_{K-1}(0)\right\} = e^{-\mu_l}e^{\mu_l P(0;K-1,l)}$$

$$n = 0, l \leq K \leq J, 1 \leq l \leq J \tag{5b}$$

$$P(n;0,l+1) = \begin{cases} 1 & \text{for } n = 1 \\ 0 & \text{otherwise} \end{cases} \tag{5c}$$

Thus, the exact probability distribution after J stages of gain for a single electron input can be computed using Eqs. (4) and (5).

The parameters shown in Fig. 1 can be used to compute the probability distributions. Results are shown only for $b = 0$ for reasons that will become clear when comparisons with experimental data are presented in the next section. Figure 2(a) shows the log-log distribution of emitted secondary electrons for each stage of the PMT for a mean number of 2.5 photons incident on the PMT operated at 1300 V.

The recursive relation represented by Eq. (5) was carried out until stage 6. With the growing number of stages, the probability density function (PDF) rapidly converges, and beyond 5 to 6 stages very little change in the PDF occurs. The plot of Fig. 2(b) illustrates this more clearly, where along the abscissa the number of secondary electrons after n stages is normalized by the mean and the PDF values are adjusted by multiplying them by the gain. Here the first-stage output is a Poisson with a mean of 2.5 photons. The fifth and sixth stages are overlapped so well that they cannot be resolved in Fig. 2(b). This observation is consistent with the computations presented in the literature [5–7]. The kink appearing in the peak of the probability distribution is interpreted to be a resolution between 1 and 2 absorbed photons for the particular choice of b_l (zero in this case) and μ_l. Using a gamma distribution would not have shown this kink since a smooth continuous probability distribution dictated by the mean aggregate tube gain would have been predicted.

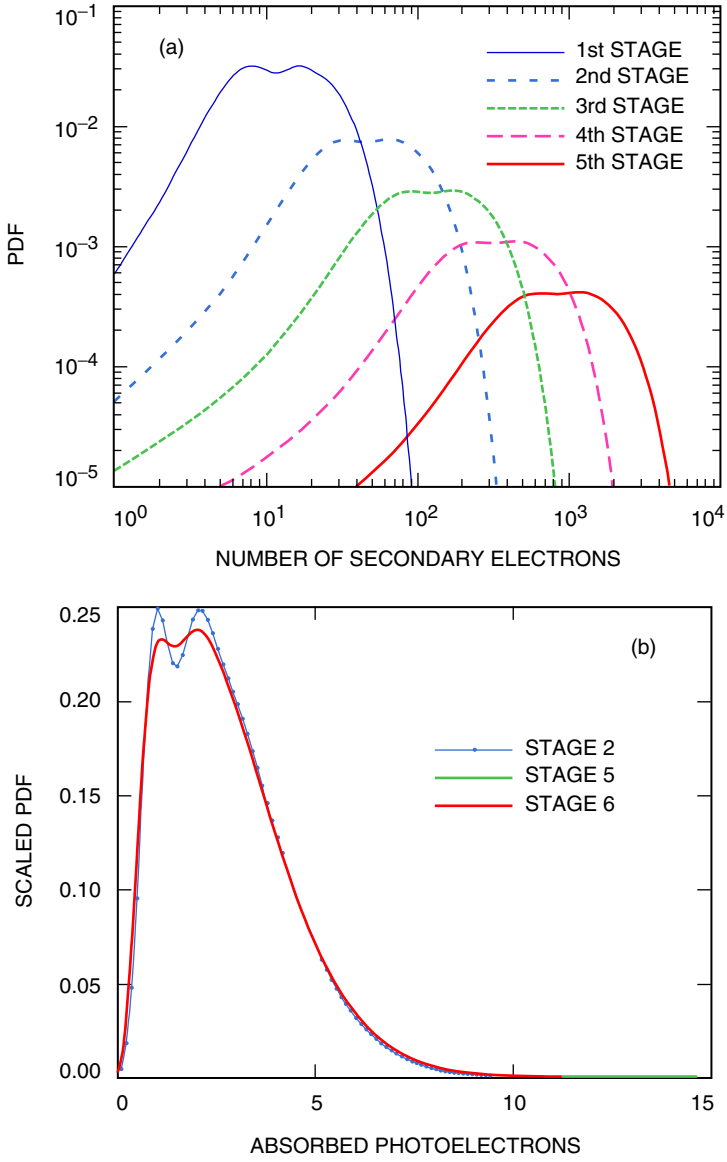

Fig. 2. Calculated PDFs using the polya-distribution model: (a) the probability distribution of the number of secondary electrons after each stage out to 6 stages of gain and (b) the rescaled stage output, showing that the probability distribution has stabilized after stage 5.

The means and standard deviations of the distribution obtained for the consecutive stages can be predicted using the simple relation

$$\sigma_{12} = \mu_2^2(\sigma_1^2) + \mu_1(\sigma_1^2) \tag{6}$$

where σ_{12} is the standard deviation after any two consecutive stages, 1,2, with means and standard deviations given by $\mu_1, \mu_2, \sigma_1, \sigma_2$, respectively. The computed data did show agreement with the relation of Eq. (6).

Figure 3 shows a composite plot for a mean of 4.8 absorbed photons on the photocathode, where the gains per stage were kept fixed, consistent with the distribution shown in Fig. 1, while the b values of the stages were varied as indicated in the legend. The significance of the variation in PDF as a result of changing b per stage will become more significant when, in Section IV, measured pulse-height distributions are compared with the model predictions.

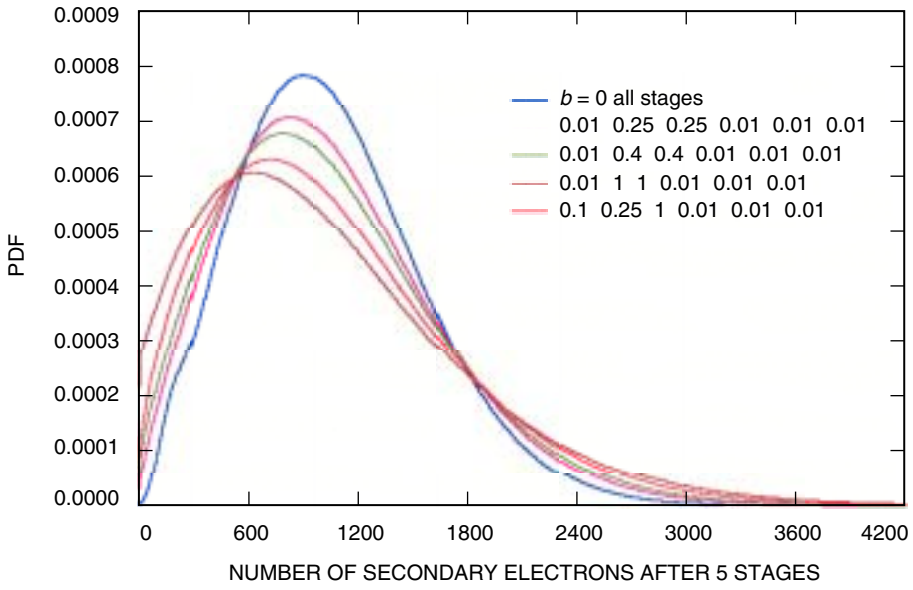

Fig. 3. The effect of changing b values for the various stages, using the gain distribution shown in Fig. 2.

III. Experimental Description

Figure 4 shows the liquid nitrogen (LN2) cooled photomultiplier tube (PMT) enclosure used for photon-counting measurements. Figure 5 shows a block diagram of the optical layout used for performing the measurements. A distributed feedback Bragg grating diode emitting single-mode light at 1070 nm serves as the source in our experiment. The laser is driven by the emitter-coupled logic (ECL) output of a Tektronix, Gigabert 1400 transmitter that can output preprogrammed word patterns. The diode output after collimation is incident upon a pellicle beam splitter. A fraction of the diode laser light is brought to incidence upon a fast (1-GHz bandwidth) New Focus, Model 1611 photodiode, the output of which is fed directly into a digital storage oscilloscope (DSO) and provides a reference laser pulse. The remaining laser beam is attenuated and guided through a shutter to a second pellicle beam splitter where the transmitted portion (almost 99.8 percent) is incident upon a power meter while the reflected portion is incident upon the PMT photocathode after passing through the narrow bandpass filter. The bandpass of the filter used for our experiment was 10 nm. A third beam splitter is shown preceding the shutter light from a broadband tungsten light source to be superimposed and propagated with the laser beam and allows the introduction of controlled amounts of white-light background noise.

For this experiment, the laser diode was aligned to ensure its incidence upon the photocathode of the PMT. Since the alignment is not possible with the PMT in place, a dummy PMT tube with an identical mechanical footprint (supplied by Hamamatsu) was used. The photocathode is not normal to the direction of laser light propagation in the experimental setup, and the incidence of the laser light is vulnerable to large amounts of backscatter with small misalignment. To address this issue, the photocathode illuminated by the 1070-nm laser spot of the dummy device was imaged on a charged-coupled device (CCD) camera (not shown in Fig. 5). Fine adjustments were made with this arrangement

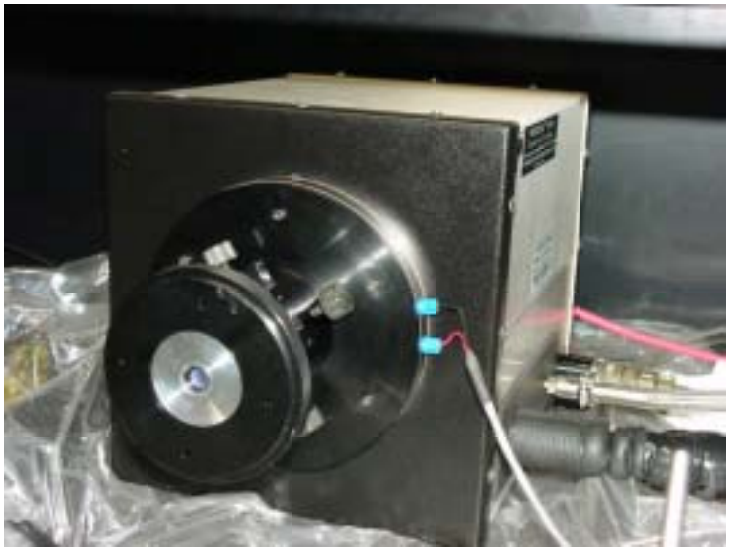

Fig. 4. The PMT assembly enclosed in the liquid nitrogen enclosure. Light incident on a narrow bandpass (10-nm) filter is transmitted to the PMT photocathode through an evacuated window. The evacuated window is heated to prevent condensation when the PMT is cooled.

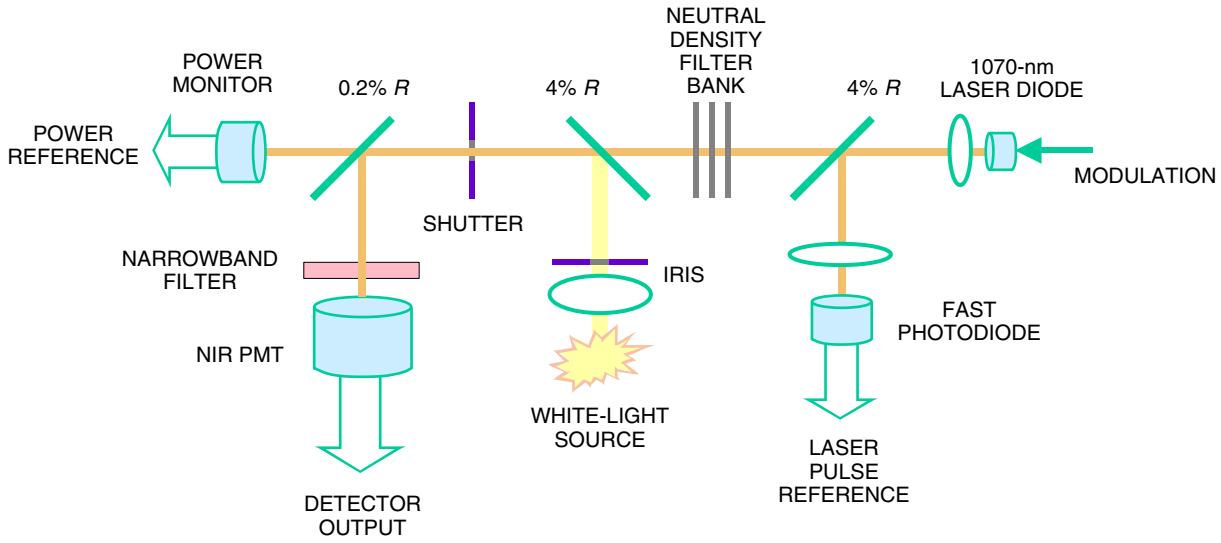

Fig. 5. Representation of the optical arrangement used during the experiment.

to ensure a minimum in backscattered laser light. Furthermore, with the dummy tube removed, the light transmitted through the narrow-bandpass filter and the vacuum window was measured so that the exact splitting ratio at the pellicle beam splitter could be determined. The laser power incident on the PMT was found to be 0.00126 times the power measured by the power meter.

Table 2 shows the tube characteristics and the laser driver settings used for performing measurements. Figure 6 shows an example of the bit patterns used to generate various 4-PPM (4-slot) words. Most of the data were gathered using a sequence of zeros.

The laser pulse width was set to half the slot width. The PMT was operated at the maximum data rate achievable while the PMT was at its anode current limit. In addition to 4-PPM, some 8-PPM (8-slot)

data also were gathered, as shown in Table 2. With the laser turned on and modulated by the Gigabert transmitter, the output of the photodiode was stored on one channel of the DSO (4 MB or records), while simultaneously the PMT output, after preamplification by a low-noise bipolar operational amplifier-based circuit, was stored on a second channel of the DSO. The sampling rate used on the DSO was set to a harmonic of the slot rate.

IV. Results

Figure 7 shows a typical data set, with the top trace showing the high-speed photodiode output marking the incident pulses, while the lower trace shows the PMT output following preamplification. The sampling used for the data of Fig. 7 was 250 megasamples per second. The data were processed using MATLAB routines where a sequence of time markers corresponding to the occurrence of the photodiode outputs was extracted and stored. Next taking into account the mean delay between the photodiode and PMT pulses, the PMT data sequence is binned according to the M-PPM signaling scheme. The sum of the voltage in each of the 2^M slots comprising each M-PPM symbol was determined, and then the maximum slot for each PPM symbol was determined. A comparison of the maximum slot with the reference file containing the photodiode output pulse then was made, and the fraction of agreements was taken as the

Table 2. The tube characteristics and laser driver settings used for performing measurements.

Characteristic/setting	Tube voltage		
	1500 V	1300 V	1300 V
Gain	6.0×10^5	2.0×10^5	2.0×10^5
Maximum cathode, electrons	20.8×10^6	125.0×10^6	125.0×10^6
Mean absorbed photons/pulse	8	8	8
Maximum pulse rate	7.8 MHz	15.6 MHz	25 MHz
Word time	128 ns	64 ns	40 ns
Slot width	16 ns	16 ns	10 ns
Encoding	8-PPM	4-PPM	4-PPM
Data rate	23 Mb/s	31 Mb/s	50 Mb/s

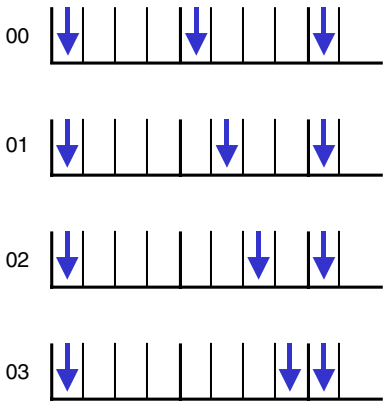

Fig. 6. The bit patterns used to generate 4-PPM words.

correctly detected words yielding a symbol- or word-error rate (WER). In addition, the peaks of all the maximum slots also were recorded, and a pulse-height distribution or histogram could be determined; 7 effective bits were used for binning the pulse-height histogram data.

Figure 8 shows a plot of the mean number of photons per pulse versus the pulse height in volts for the pulse-height distribution determined for a varying number of incident photons. The mean pulse height was determined for a mean of 250,000 pulses. The standard deviation of the pulse heights increases with the mean number of detected photons, indicative of a Poisson nature of the photoelectron statistics.

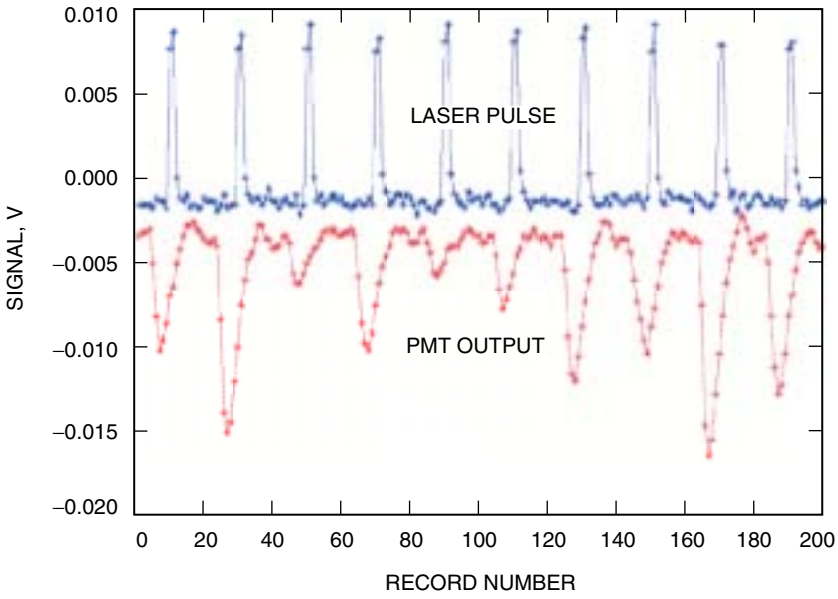

Fig. 7. Typical data set, with the top trace of the DSO showing the reference high-speed photodiode output and the lower trace showing the PMT output. Data were sampled at 250 Msamples per second.

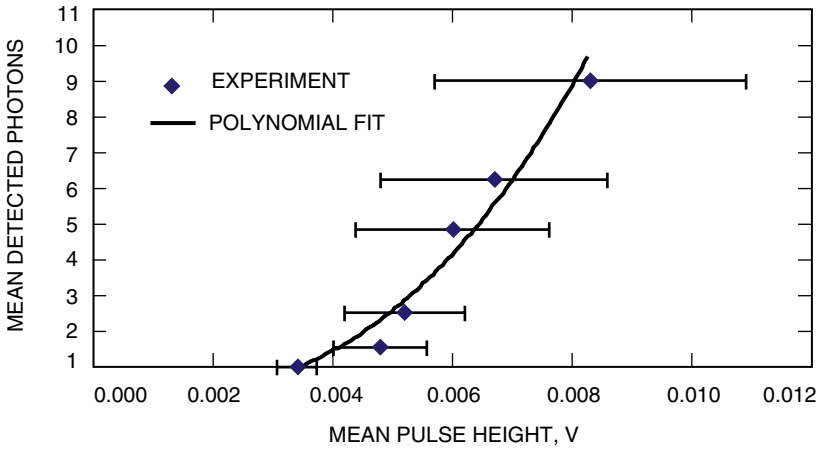

Fig. 8. The mean pulse height for 250,000 pulses versus the mean number of incident photons on the PMT. A power relation best fits the experimental data. The x-error bars are the standard deviation of the distribution. The increase in variance with an increasing number of photons is indicative of a Poisson nature.

Figure 9 shows a comparison of the actual measured pulse-height histogram compared with the Polya distribution for 4.8 mean detected photons. The fit was obtained by free fitting the b values for each stage of the PMT shown in Fig. 2. The fact that the first stage (photocathode) requires a $b = 0.1$ in order to bring the experiment and prediction within reasonable agreement suggests that the spatial gain of the photocathode is not uniform. If it were uniform, the first stage would have had a pure Poisson distribution, or $b = 0$. The first and second dynode stages that have high gain associated with them appear to have even more spatial nonuniformities in the gain, indicated by b values of 0.25 and 1.0, respectively. The subsequent gain stages have lower gain and appear to behave very Poisson-like because the b value for these stages was 0.01.

Figure 10 shows the bit-error-rate (BER) measurements obtained by processing the data using the method described above. The measurements using 1500 V on the PMT could not be carried out to a lower BER because the anode current limit was reached already. The 1300-V measurements suggest that backing off on the gain allows operating at lower BERs without saturating the PMT, although at a reduced performance. The measured BER plots are compared with a lower Poisson bound. In future analysis, the BER curves will be derived based upon the Polya distribution presented in this article. Based upon the 8 photons per pulse required to achieve a 10^{-2} BER, the bits per photon range from 0.25 to 0.42 for the 4- and 8-PPM.

The following observations can be made about the bits/detected photon achieved in the current article versus the 2.5 bits/detected photon reported in [1,2]. In terms of mean detected photons per pulse, our results show 7 and 8 detected photons for an uncoded BER of 0.02. In our work, we lowered the PPM order in order to demonstrate higher data rates; however, if we used the same slot widths (16 ns) with 256-PPM, we would have lowered our data rate to 1.95 Mb/s with 1 to 1.1 bits/detected photon. Note that in [2] the PMT gains ranged from 6×10^5 to 10^7, compared to 2×10^5 to 6×10^5 in the current work. In [2], 1.3 bits/detected photon were obtained for the lowest gain, which is equivalent to the highest gain of the current device. As for the discrepancy of 1.3 versus 1.1, the bandwidth of our receiver (16-ns slots) is higher than that of [2] (100-ns slots) and hence more vulnerable to noise. So the 0.25- to 0.42-bit/detected photon performance shown for the current PMT device is consistent with previously observed 2.5 bits/detected photon when the the PMT gain and higher data rate and bandwidths are accounted for.

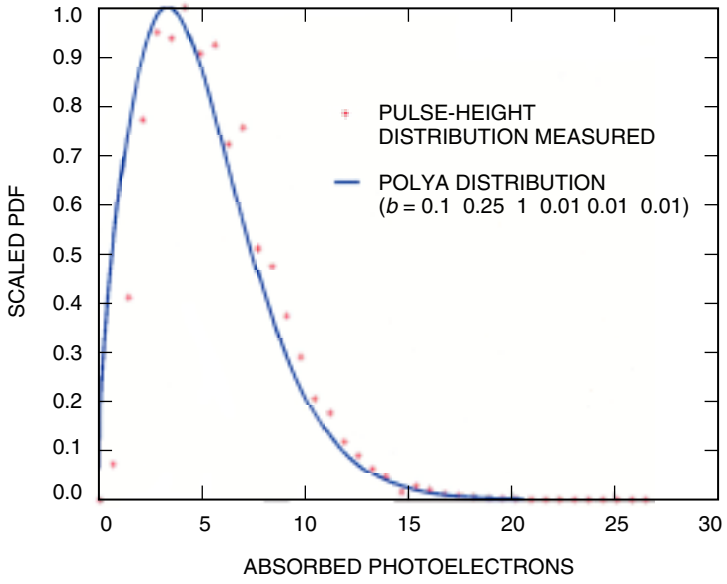

Fig. 9. A comparison of the measured pulse-height distribution with the computed Polya distribution using the stage gains shown in Fig. 2 and the b values shown in the legend.

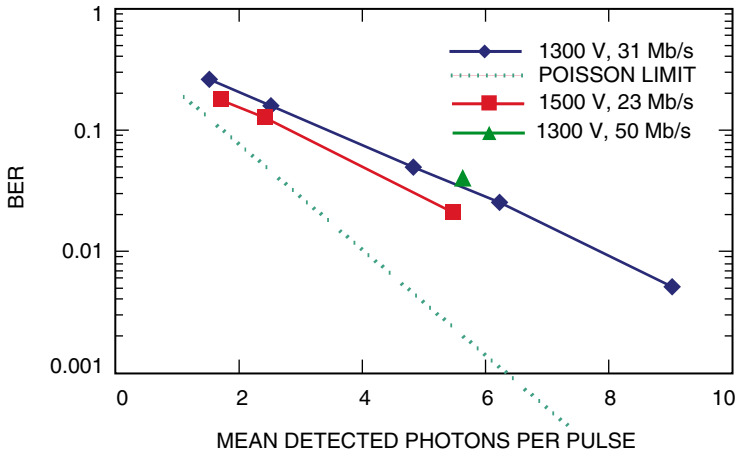

Fig. 10. The measured bit-error rates compared to a lower bound of a purely Poisson process.

V. Conclusion

In the work presented, a near-infrared enhanced photomultiplier tube was modeled using a discrete Polya distribution in order to compute the probability distribution function of the electrons generated after a dynode chain. The model takes into account individual stage gains and furthermore allows a shape parameter to be used for each dynode stage that represents the spatial uniformity of the response for that stage. Experiments were performed to generate a sequence of on–off key laser pulses that are timed in a manner that could be interpreted as all zeros for 4-PPM and 8-PPM. The PMT output was stored in a DSO, and post-analysis was used to determine the pulse-height distribution as well as the BER dependence on the mean number of photons incident.

In future work, the BER for a PPM pulse sequence incident on the PMT will be derived using the Polya distribution model as well as taking into account the effect of background and dark noise. The agreement shown in the model and measured data will alxo be tested further.

References

[1] J. R. Lesh, J. Katz, H. H. Tan, and D. Zwillinger, "2.5-Bit/Detected Photon Demonstration Program: Description, Analysis, and Phase I Results," *The Telecommunications and Data Acquisition Progress Report 42-66, September and October 1981,* Jet Propulsion Laboratory, Pasadena, California, pp. 115–132, December 15, 1981.
http://tmo.jpl.nasa.gov/tmo/progress_report/42-66/66P.PDF

[2] J. Katz, "2.5 Bit/Detected Photon Demonstration Program: Phase II and III Experimental Results," *The Telecommunications and Data Acquisition Progress Report 42-70, May and June 1982,* Jet Propulsion Laboratory, Pasadena, California, pp. 95–104, August 15, 1982.
http://tmo.jpl.nasa.gov/tmo/progress_report/42-70/70J.PDF

[3] H. H. Tan, "A Statistical Model of the Photomultiplier Gain Process With Applications to Optical Pulse Detection," *The Telecommunications and Data Acquisition Progress Report 42-68, January and February 1982,* Jet Propulsion Laboratory, Pasadena, California, pp. 55–67, April 15, 1982.
http://tmo.jpl.nasa.gov/tmo/progress_report/42-68/68H.PDF

[4] R. J. Stokey and P. J. Lee, "Approximation to the Probability Density at the Output of a Photomultiplier Tube," *The Telecommunications and Data Acquisition Progress Report 42-73, January–March 1983,* Jet Propulsion Laboratory, Pasadena, California, pp. 36–39, May 15, 1983.
http://tmo.jpl.nasa.gov/tmo/progress_report/42-73/73D.PDF

[5] R. W. Engstrom, *RCA Photomultiplier Handbook,* RCA, 1980.

[6] J. R. Prescott, "Statistical Model for Photo-Multiplier Single-Electron Statistics," *Nucl. Instrum. and Methods,* vol. 39, pp. 173–179, 1966.

[7] L. A. Dietz, L. R. Hanrahn, and A. B. Hance, "Single-Electron Response of a Porous KCL Transmission Dynode and Application of Polya Statistics to Particle Counting in an Electron Multiplier," *Rev. Sci. Instrum.,* vol. 38, pp. 176–183, 1967.